

## Supplementary Materials

### Self-Assembly Mechanism of Complex Corrugated Particles

Lanqin Tang,<sup>1,2,3#</sup> Thi Vo,<sup>2,3#</sup> Xiaoxing Fan,<sup>2,4</sup> Drew Vecchio,<sup>2</sup> Tao Ma,<sup>5,6</sup> Jun Lu,<sup>2,3</sup>  
Harrison Hou,<sup>2,3</sup> Sharon C. Glotzer,<sup>\*,2,3</sup> Nicholas A. Kotov<sup>\*,2,3</sup>

<sup>1</sup> Department of Chemistry and Chemical Engineering, Yancheng Institute of Technology, Yancheng, Jiangsu 224051, P. R. China;

<sup>2</sup> Department of Chemical Engineering, University of Michigan, Ann Arbor, MI, 48109, USA;

<sup>3</sup> Biointerfaces Institute, University of Michigan, Ann Arbor, MI, 48109, USA;

<sup>4</sup> School of Physics, Liaoning University, Shenyang, Liaoning 110036, P. R. China;

<sup>5</sup> Michigan Center for Materials Characterization, University of Michigan, Ann Arbor, MI 48109-2102, USA;

<sup>6</sup> Department of Materials Science, University of Michigan, Ann Arbor, MI, 48109, USA.

\*Corresponding authors: [sglotzer@umich.edu](mailto:sglotzer@umich.edu); [kotov@umich.edu](mailto:kotov@umich.edu)

# These authors contributed equally.

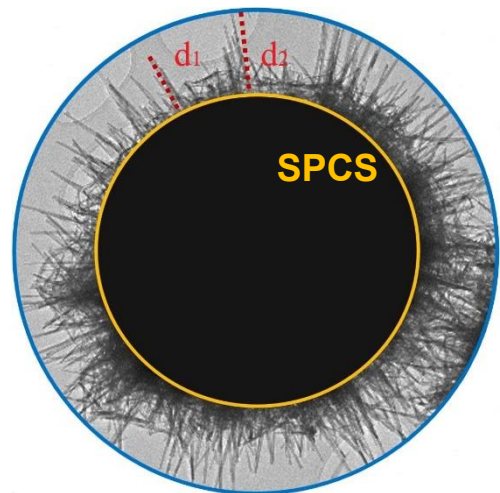
#### Additional Characterization Methods:

Scanning electron microscopy (SEM) images and energy-dispersive X-ray (EDX) spectroscopy data were acquired by a FEI Helios Nanolab 650 Dual-beam system. Transmission electron microscopy (TEM) and high-resolution scanning transmission electron microscopy (HR-STEM) images were obtained using a JEOL-3100R05 double-corrected S/TEM operated at 300 kV. Element-mapping and tomography series were carried out using a Thermo Fisher Scientific Talos F200X G2 S/TEM equipped with a Super-X EDX detector. The tomography dataset was acquired by tilting the sample from -70° to 70° with an increment of 2°. The 3D reconstruction was performed with the simultaneous iterations reconstruction technique (SIRT) algorithm using the reconstruction module in Gatan Digital Micrograph. Powder X-ray diffraction (XRD) experiments were performed on a Rigaku rotating anode X-ray diffractometer using Cu K $\alpha$  radiation (1.54 Å) to determine the crystal structure of the nanocrystals. Raman spectra were obtained on a Renishaw inVia microscope at room temperature (Ar

ion laser, 532 nm). Optical absorption spectra were measured at room temperature using an Agilent 8453 UV-Vis spectrophotometer.

The reported length of the spikes corresponds to their visible portion and was calculated based on the TEM images as the average statistically processed distance between the circumference describing *supraparticle of critical size* (SPCS) and the ends of the spikes (**Schematics**

1). The diameter of spikes was calculated from the analysis of TEM images based on at least 30 spikes are analyzed with the assistance of software named “Nano Measurer”, the diameter of each spike was measured three times.



**Schematics 1.** Description of the measurements of the spike lengths from TEM images.

The number of spikes per  $\mu\text{m}^2$  was obtained from the analysis of SEM images. Spikes within a  $1\ \mu\text{m} \times 1\ \mu\text{m}$  square area were counted three times. A total of ten different areas were analyzed to obtain the average.

### Energy of SPCS and corrugated particles.

To determine the critical size,  $R_c$ , of SPCS, we consider the potential energy balance of the NP assembly comprised of  $n$  NPs as the size of the assembly approaches  $R_c$ . The energy of attractive van der Waals interactions within a SPCS is  $\sim \nu\phi$ ,<sup>1</sup> where  $\nu$  is the excluded volume associated with a single NP – that is, the space inaccessible to an approaching new NP due to the presence of another NP occupying that space – and  $\phi$  is the concentration inside the SPCS:  $\phi = n/R_c^3$ . Physically this relation describes the following situation. Assuming that NPs are uniformly distributed inside the

SPCS, the probability that a NP within this assembly (the “reference particle”) will interact with another NP near it is  $n/R_c^3$ . As a result, the energy per particle due to van der Waals attraction is the product of the probability of finding the reference NP’s range of interaction (i.e., its excluded volume,  $v$ ) and the probability of finding another NP ( $n/R_c^{-3}$ ), resulting in  $vn/R_c^{-3} \sim v\phi$ .

We consider now a growing assembly to which one more NP is added so that the total number of NPs in the assembly becomes  $n + 1$ . Approximating electrostatic repulsion by a Yukawa potential for screened Coulombic interactions, the critical size  $R_c$  of the assembly (where the SP becomes the SPCS) is defined by the balance between the two opposing interactions – van der Waals and Yukawa

$$v\phi = k_r(n + 1) \frac{e^{-\kappa R_c}}{R_c/\sigma} \quad (1)$$

where  $k_r$  is a scaling constant for the amplitude of the repulsion and is inversely related to the dielectric constant at the interface of the SPCS,  $\kappa$  is the inverse of the Debye screening length of the electrolyte around the NP, and  $\sigma$  is the dimensionality conversion constant commensurate with the units of  $\kappa$  and  $R_c$ . Rearranging Eq. 1 gives Eq. 2, which can be solved numerically for  $R_c$

$$[1 + n]R_c^2\sigma v^{-1}e^{-\kappa R_c} - n \sim 0 \quad (2)$$

When the size of the assembly becomes larger than  $R_c$ , the assumption of a constant  $v$  is no longer valid as the electrostatic forces now select NPs with sizes whose net charge falls within the range that enables continued particle growth – that is, where the van der Waals interactions between a new NP and that particles in the assembly near the addition site are stronger than the corresponding electrostatic repulsion. To help with clarity, we will refer to the growing SP with size  $R < R_c$  and  $R > R_c$  as  $\text{SP}_{\text{pre}}$  and  $\text{SP}_{\text{post}}$ , respectively. Let us define  $\xi$  as the size of NPs being added at a specific distance from the

surface of the growing aggregate. The correlation size  $\xi$  can be defined by balancing van der Waals attraction driving NP attachment and electrostatic repulsion. Here, we take the standard scaling form for van der Waals attraction  $U_{vdw} \sim C/\xi^6$  and a Yukawa screened potential for electrostatic repulsion  $U_{yukawa} \sim n_c n_x / \xi / \sigma e^{-\kappa \xi}$ , where  $n_c$  is the charge contribution from the growing SP<sub>post</sub>,  $n_x$  is the charge contribution from the NP, and  $C$  is London coefficient of the particle-particle interaction potential. Noting that  $C$  is related to the Hamaker constant via the relationship  $A \sim \pi^2 k_B T C \rho_1 \rho_2$ , we can substitute  $A$  for  $C$  in  $U_{vdw}$  and define  $U_\xi \sim U_{vdw} + U_{yukawa}$  to give

$$U_\xi \sim \frac{n_c n_x}{\xi / \sigma} e^{-\kappa \xi} + \frac{A}{T \xi^6} \quad (3)$$

where we dropped unitary constants such as  $\pi$ ,  $k_B$ , and  $\rho$ . By representing the charge contribution in terms of the number of NPs, we are implicitly assuming that the net charge scales linearly with the number of NPs. Minimization of Eq. 3 for  $\xi$  gives

$$\xi \sim A^{1/5} T^{-1/5} \kappa^{1/5} (n_T - n_x)^{-1/5} n_x^{-1/5} \quad (4)$$

where  $n_T = n_c + n_x$  is the total charge in the growing particle assembly after successful NP addition. Minimizing Eq. 3 to obtain  $\xi$  represents solving for the closest distance with which a NP from solution can be positioned relative to the SP<sub>post</sub> growth front so that the electrostatic repulsion pushing the NP back into solution is balanced out by the van der Waals attraction holding it in place. By definition, the excluded volume dependency of the NP is simply  $v \sim \xi^3$ . To a first-order approximation,  $n_T \gg n_x$  (especially as the SP grows) and  $n_x \sim 1$ . Thus, we can write

$$\xi \sim A^{1/5} T^{-1/5} \kappa^{1/5} n_T^{-1/5} \quad (5)$$

To determine the dependence of  $n_T$  on the distance away from the surface of the SPCS, we

employ geometry concepts commonly used to treat polymeric systems<sup>2,3</sup>. The physical picture underpinning our theoretical development is such successive stacking of NPs of decreasing sizes form tapered spikes. Geometrically, such spikes are analogous to conical frustums growing from the surface of an SPCS. Therefore, we can write the total number of NPs within the growing  $SP_{\text{post}}$  as  $n_T \sim \xi^2 r \sigma^{-3}$ . Rearranging  $n_T$  for  $\xi$ , plugging  $\xi$  into the left hand side of Eq. 5, and solving for  $n_T$  gives

$$n_T(r) \sim A^{2/7} T^{-2/7} \kappa^{2/7} r^{1/7} \sigma^{-1/7} \quad (6)$$

Substituting Eq. 6 into Eq. 5 gives

$$\xi(r) \sim A^{1/7} T^{-1/7} \kappa^{1/7} r^{-1/7} \sigma^{3/7} \quad (7)$$

Lastly, the concentration of NPs can then be written as  $\phi \sim n_T \sigma^3 (R_c + \xi)^{-2} r^{-1}$ . Using Eq. 2 for  $R_c$  and plugging in Eqs. 6 and 7 for  $\xi$  and  $n_T$ , respectively yields

$$\phi(r) \sim [R_c A^{-1/7} T^{1/7} \kappa^{-1/7} r^{1/7} \sigma^{-3/7} + 1]^{-2} \quad (8)$$

The potential energy of adding NPs to the  $SP_{\text{post}}$  growth front when electrostatic repulsion dominates the growth can be written as

$$U(r) \sim \xi^3(r) \phi(r) + \frac{n_T(r)}{r/\sigma} e^{-\kappa r} \quad (9)$$

where  $n_T(r)$ ,  $\xi(r)$ , and  $\phi(r)$  are defined by Eq 6, 7, and 8, respectively. Eq. 9 can be used to carry out the Monte Carlo (MC) simulations to test the theory's ability to predict the various experimentally observed NP assemblies.

We can employ Eq. 9 to define the crossover condition (where  $U(r) = 0$ ) as  $\xi^3 \phi \sim n_T r^{-1} \sigma e^{-\kappa r}$ .

Plugging in Eq. 6, 7, and 8 for  $n_T$ ,  $\xi$ , and  $\phi$ , respectively and rearranging yields Eqs. 10 and Eq. 11 for the  $NR_A \rightarrow HP$  and  $HP \rightarrow$  low corrugation particles transitions, respectively.

$$\kappa^{-1/14} \sim A^{-2/7} T^{-12/7} \quad (10)$$

$$\kappa^{-1/7} \sim A^{-2/7} T^{-12/7} \quad (11)$$

These results suggest that a log-log plot of  $\kappa$  versus  $A^{-2/7} T^{-12/7}$  should yield a straight line with a slope of  $-31/14$  and  $-5/7$  at the  $NR_A \rightarrow HP$  and  $HP \rightarrow$  low corrugation particles transitions, respectively. **Figure 11b** confirms that the theory predicts the experimentally observed behavior across all four pertinent classes of self-assembled morphologies reported in **Figure 1**. Note that low-corrugation particles do not imply that they *necessarily* have lower complexity. In our case, they are FLP, but can also be simple spherical SPs observed in many other instances.

### Extension to FLPs

The model encapsulated in Eqs. 5–9 operates in the limit without reaction rate and /or diffusion limitations: that is, without effects of hydrodynamics. There, once a NP of the correct size (and thus charge) finds its way to the  $SP_{\text{post}}$  growth front, it will always be added to the growing particle. However, there can be situations where either the attachment reaction rate is too slow or diffusion is too fast, causing NPs to diffuse away from the  $SP_{\text{post}}$  growth front before it can attach to the growing particle. As such, the attachment probability of a NP with the correct size attaching to the  $SP_{\text{post}}$  is not necessarily 1. Such hydrodynamic effects can reduce corrugation in the resultant particle as well as change the spike shape, favoring the formation of FLPs. In other words, how fast a particle attaches to the  $SP_{\text{post}}$  modulates the formation of HPs vs FLPs.

We start by incorporating the effects of diffusion into the theory. For an NP of size  $\xi$  near a growth point, the viscous drag force favoring attachment has the following form  $F_D \sim 6\pi\eta v\xi^2/l$ , where  $\eta$  is the fluid viscosity,  $v$  is the velocity of the growing front, and  $l$  is the distance between the NP and the  $\text{SP}_{\text{post}}$  front.<sup>4</sup> The interfacial energy change of an NP “leaving” the solution to attach to the  $\text{SP}_{\text{post}}$  takes the form  $F_\sigma \sim 2\pi\xi(U_{\text{att}} - U_{\text{rep}})$ , where  $U_{\text{att}}$  and  $U_{\text{rep}}$  are the attractive and repulsive interactions, respectively.<sup>4</sup> Since we are interested in behaviors at the contact between a NP and  $\text{SP}_{\text{post}}$ , typical values of  $l$  are such that  $l \ll \xi$ . Additionally,  $U_{\text{att}} \sim A/T r^6$  and  $U_{\text{rep}} \sim n_T \delta^{2\pm}/r$ . Equating  $F_\sigma = F_D$  and solving for  $v$  gives the critical velocity,  $(v^*)$ , at which the effect of hydrodynamics influences the growth mechanism of the SP

$$v_H^* \sim \left(\frac{l}{\xi\eta}\right) \left(\frac{A}{Tr^6} - \frac{n_T \delta^{2\pm}}{r}\right) \quad (12)$$

Physically,  $v < v^*$  means that the  $\text{SP}_{\text{post}}$  growth front is moving too slowly. As such, NP can diffuse away from the  $\text{SP}_{\text{post}}$  surface and not attach to the growth front. Conversely, for  $v > v^*$ , the  $\text{SP}_{\text{post}}$  exhibit a fast growth rate and NPs readily attach to the  $\text{SP}_{\text{post}}$  before they can diffuse away. Furthermore,  $v^*$  gives the characteristic scaling behavior for how the growth front speed depends on systems parameters such as  $A$ ,  $T$ , and  $\xi$ . We can directly quantify the number of NPs that adds to the front as  $n_H \sim \xi r v^* \Delta t$ . We now add  $n_H$  to Eq. 6 to obtain the total number of NPs in the  $\text{SP}_{\text{post}}$ :  $n_T \sim A^{2/7} T^{-2/7} \kappa^{2/7} r^{5/7} \sigma^{-15/7} + n_H$ . Note that  $\xi$  in  $n_H$  also depends on  $n_T$  (Eq. 5). Therefore, we plug in  $\xi$  and  $v^*$  and solve for  $n_T$  to give

$$n_T(r) \sim \frac{A^{2/7} T^{-2/7} \kappa^{2/7} r^{5/7} \sigma^{-15/7} + A l \eta^{-1} r^{-5} \Delta t}{1 + l \eta^{-1} \Delta t} \quad (13)$$

To approximate the behavior of  $\Delta t$ , we perform the following reaction kinetics scaling analysis. The

surface area  $A_S$  of the  $\text{SP}_{\text{post}}$  growth front increases with time  $t$ , giving  $A_S \sim \Delta t^\gamma$ . Here  $\gamma \geq 1$  to indicate a growth of the  $\text{SP}_{\text{post}}$ . A higher  $\gamma$  indicates faster  $\text{SP}_{\text{post}}$  growth and therefore a faster reaction rate. Therefore,  $\gamma$  can be interpreted as the reaction rate for NP attachment to the  $\text{SP}_{\text{post}}$  growth front. The distance away from the surface of  $R_c$  also defines the surface area of the  $\text{SP}_{\text{post}}$  growth front:  $A_S \sim r^2$ . Substituting for  $A_S$  then gives  $\Delta t \sim r^{1/\gamma}$ . Plugging  $\Delta t$  into Eq. 13 gives

$$n_T(r) \sim \frac{A^{2/7} T^{-2/7} \kappa^{2/7} r^{5/7} \sigma^{-15/7} + A l \eta^{-1} r^{1/\gamma-5}}{1 + l \eta^{-1} r^{1/\gamma}} \quad (14)$$


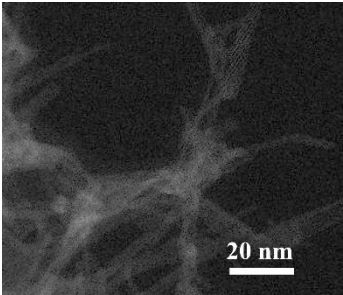

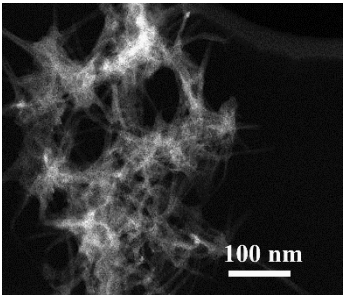

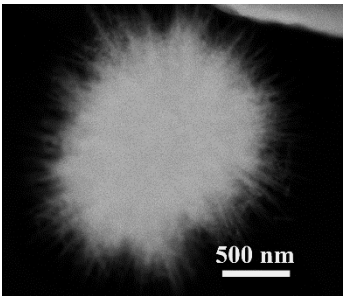
Here, it is important to note several features regarding Eq. 14 relative to Eq. 6. For fast reactions,  $\gamma \rightarrow \infty$ . The new term in the denominator reduces to a constant. The second term in the numerator becomes of order  $r^{-5}$ . Generally,  $r \gg 1$  in the regime of spike formation/growth for HPs and thus the  $r^{-5}$  term becomes negligible relative to the  $r^{5/7}$  term. As such, Eq. 14 reduces to Eq. 6 for fast reactions and we recover the formation of HPs. Eq. 14 can then be employed to define new potential energy for MC simulations.

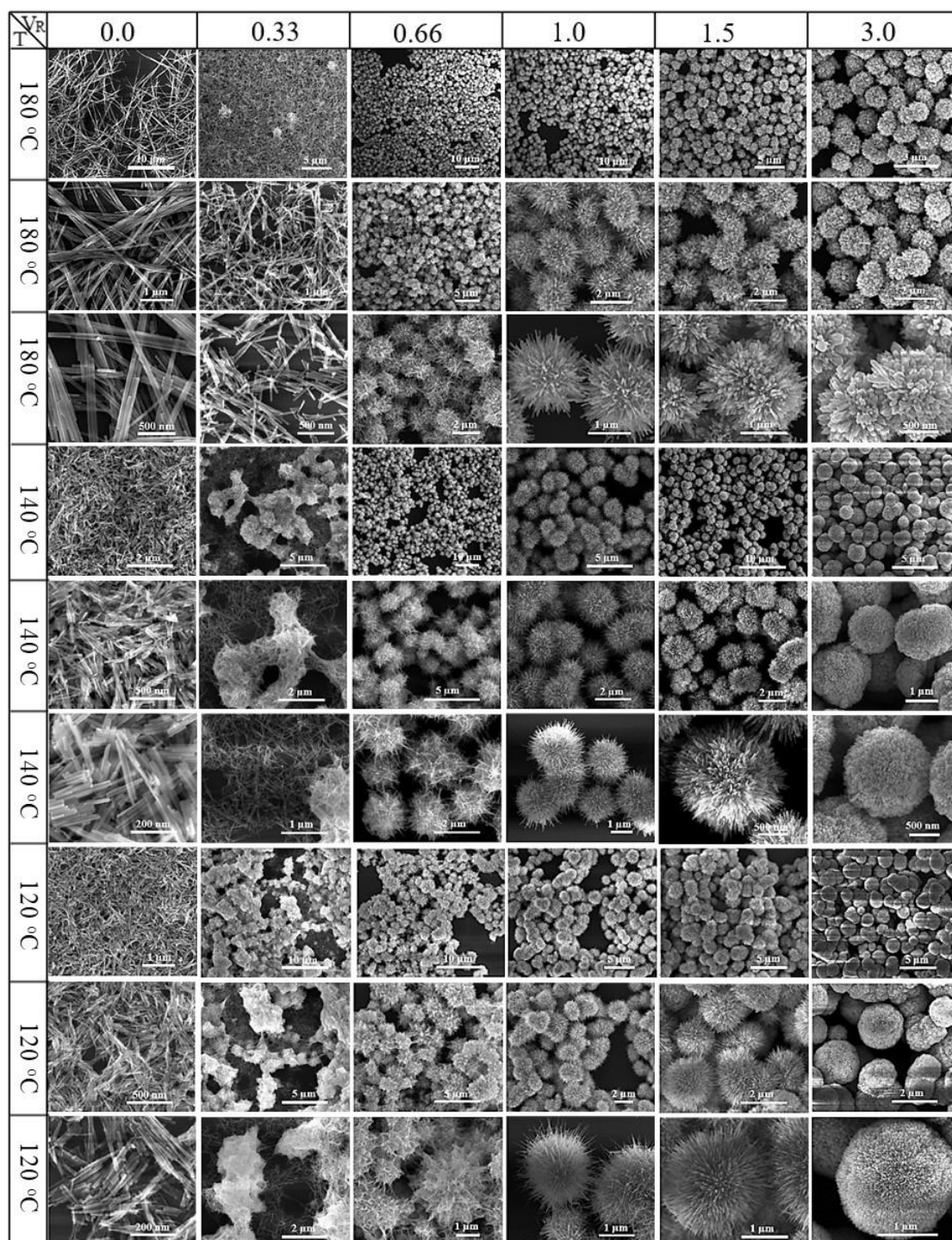
**Table S1.** Experimental parameters for the preparation of CdS nanostructures with various morphologies.

<b>Morphology</b>	<b>Volume of water (mL)</b>	<b>Volume of EA (mL)</b>	<b>Volume ratio of water to EA, <math>V_R</math></b>	<b>Reaction temperature (°C)</b>	<b>Reaction time (h)</b>
NR	0	20	0.0	180	20
NR	5	15	0.33	180	20
HP	8	12	0.66	180	20
HP	10	10	1.0	180	20
HP	12	8	1.5	180	20
FLP	15	5	3.0	180	20
NR	0	20	0.0	140	20
NR	5	15	0.33	140	20
HP	8	12	0.66	140	20
HP	10	10	1.0	140	20
HP	12	8	1.5	140	20
FLP	15	5	3.0	140	20
NR	0	20	0.0	120	20
NR	5	15	0.33	120	20
HP	8	12	0.66	120	20
HP	10	10	1.0	120	20
HP	12	8	1.5	120	20
HP	15	5	3.0	120	20

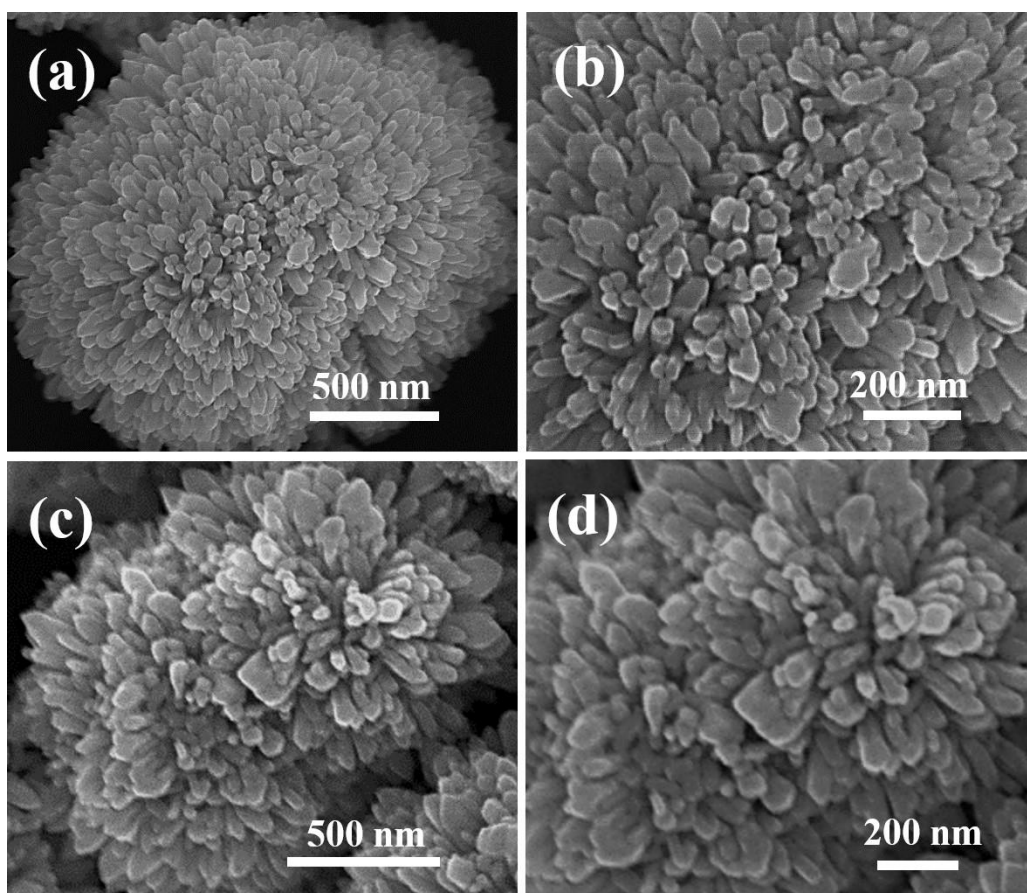
NR, HP, and FLP are abbreviations describing product morphology and refer to nanorods, hedgehog particles, and flower-like particles, respectively.

**Table S2.** CdS nanostructures forming after various reaction times.

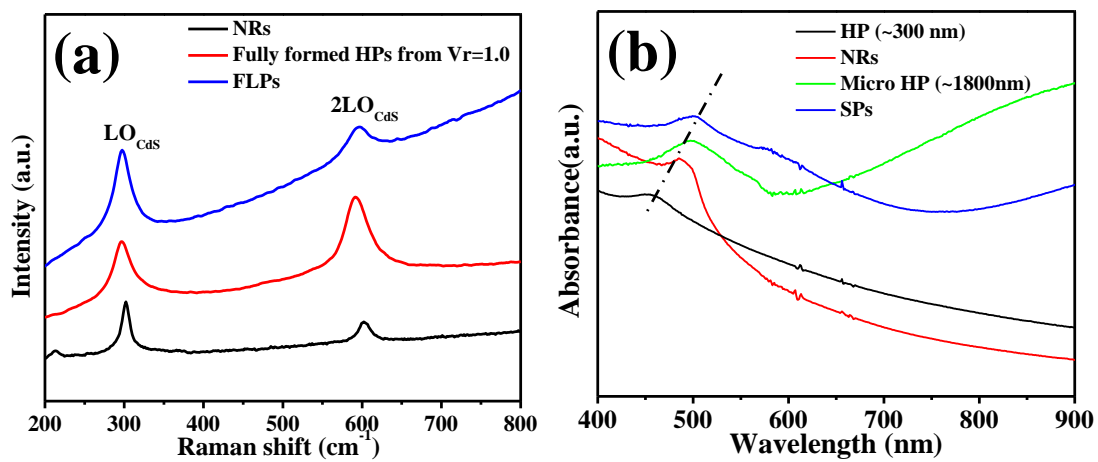
Volume of water (mL)	Volume of EA (mL)	Volume ratio of water to EA ( $V_R$ )	Reaction temperature ( $^{\circ}\text{C}$ )	Reaction time (min)	Color	Morphology
10	10	1.0	160	45		
10	10	1.0	160	55		
10	10	1.0	160	65		



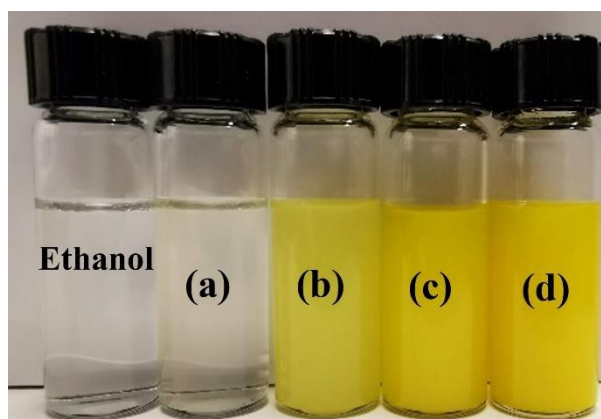
**Figure S1.** SEM images of CdS particles formed at different temperatures and  $V_R$ . Reaction time is 20 h.



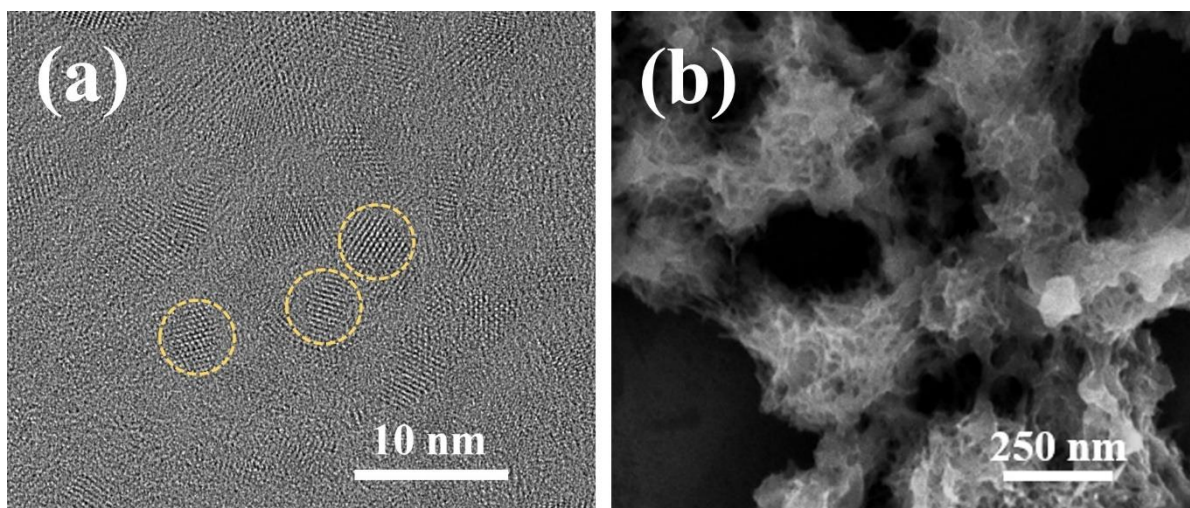
**Figure S2.** SEM images of CdS nanostructured microparticles assembled after during 20 h with  $V_R = 3.0$  at 160 °C (a, b) and 180 °C (c, d).



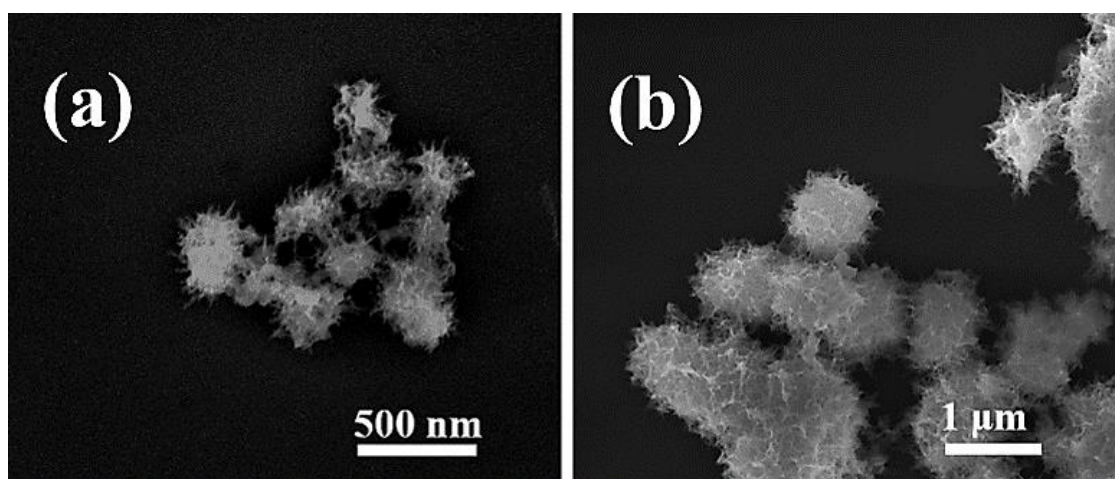
**Figure S3.** Spectroscopic characterization of HPs: (a) Raman scattering and (b) UV spectra of CdS. The corresponding sample description is given in legends.



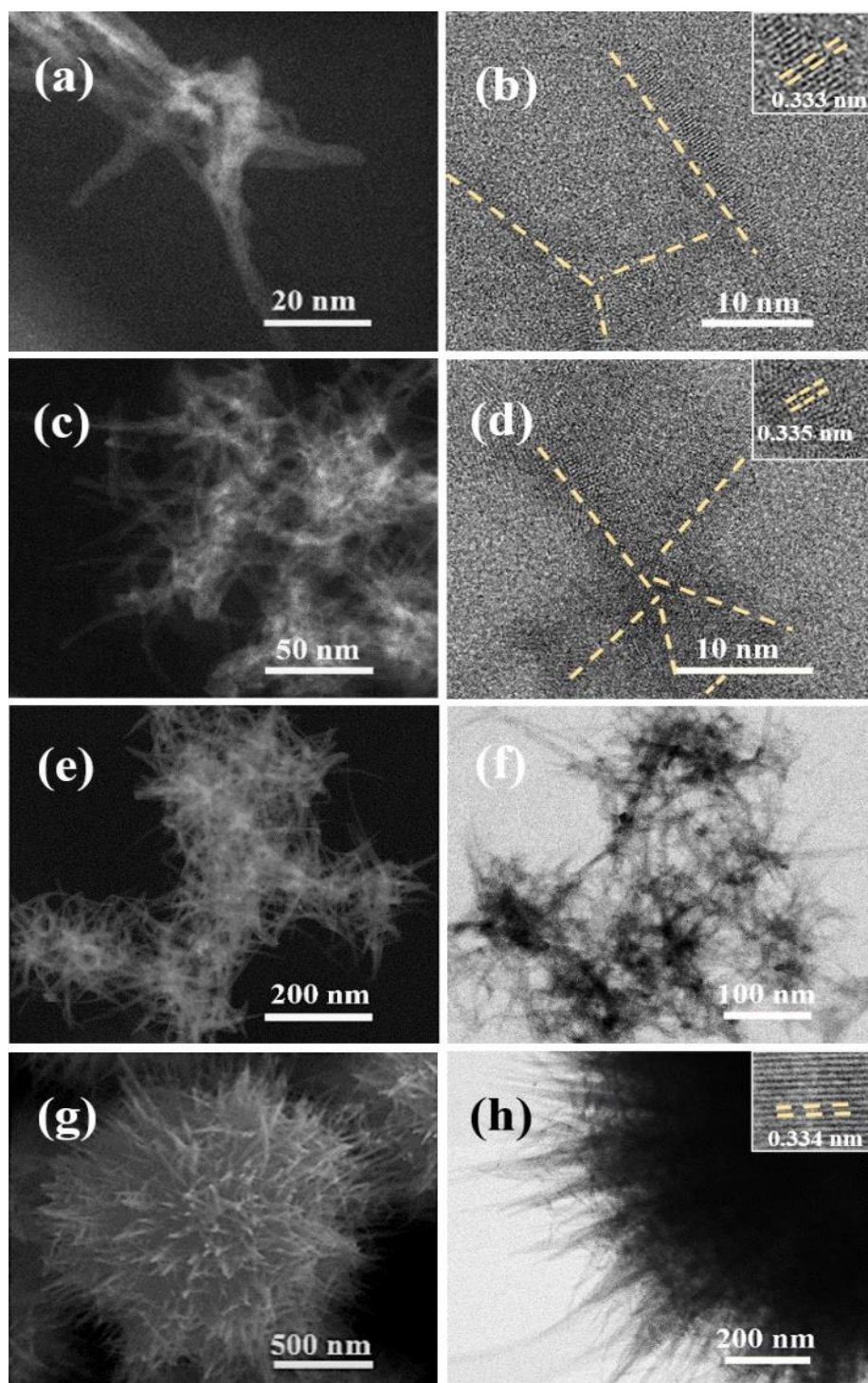
**Figure S4.** Images of CdS particle dispersions obtained at 160 °C with  $V_R = 1.0$  and different reaction times: **(a)** 45 min; **(b)** 55 min; **(c)** 65 min; and **(d)** 75 min. The color of the dispersion in the 45 min vial is light-yellow; the vial with ethanol (colorless) was put here as a comparison for color.



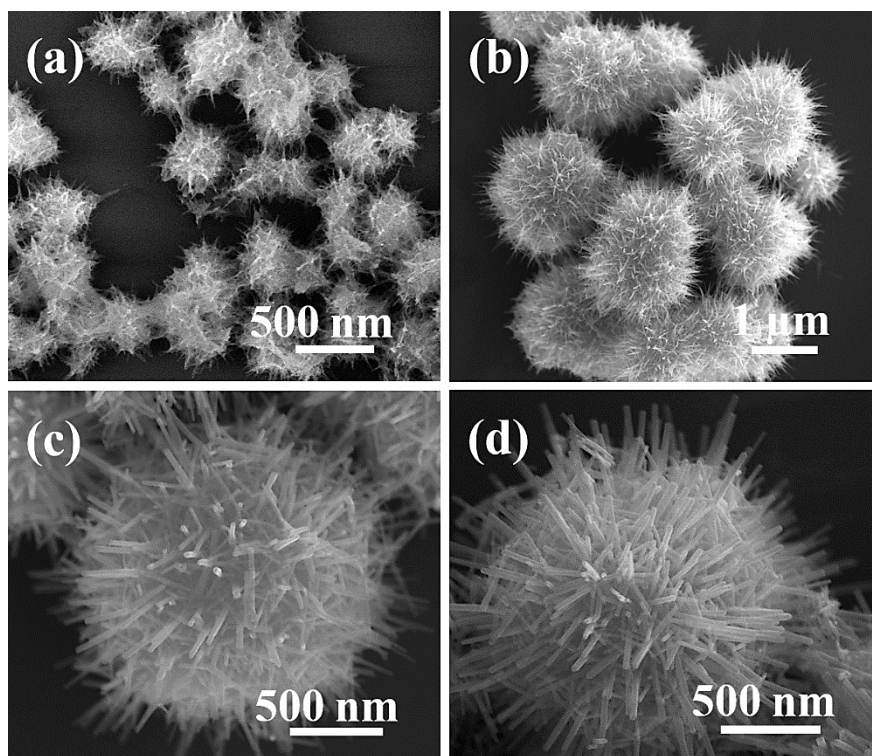
**Figure S5.** (a) NPs observed in the reaction solution incubated at 160 °C for 35 min; (b) Agglomerates observed after aging for 24 h at room temperature.



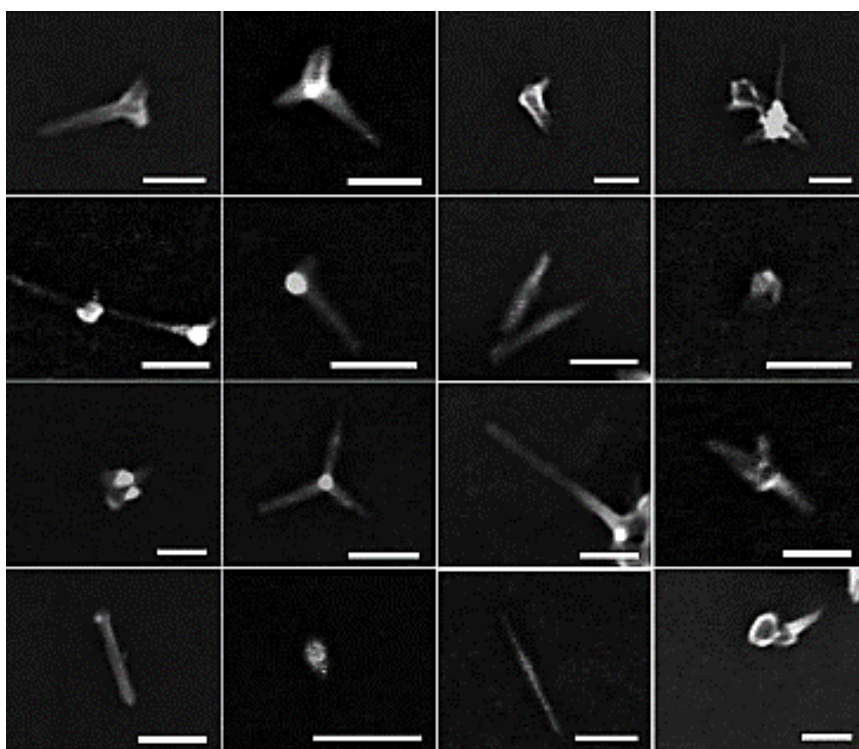
**Figure S6.** SEM images of HP-like CdS particles represented as incomplete HPs, obtained after incubation at room temperature for **(a)** three days and **(b)** two weeks.



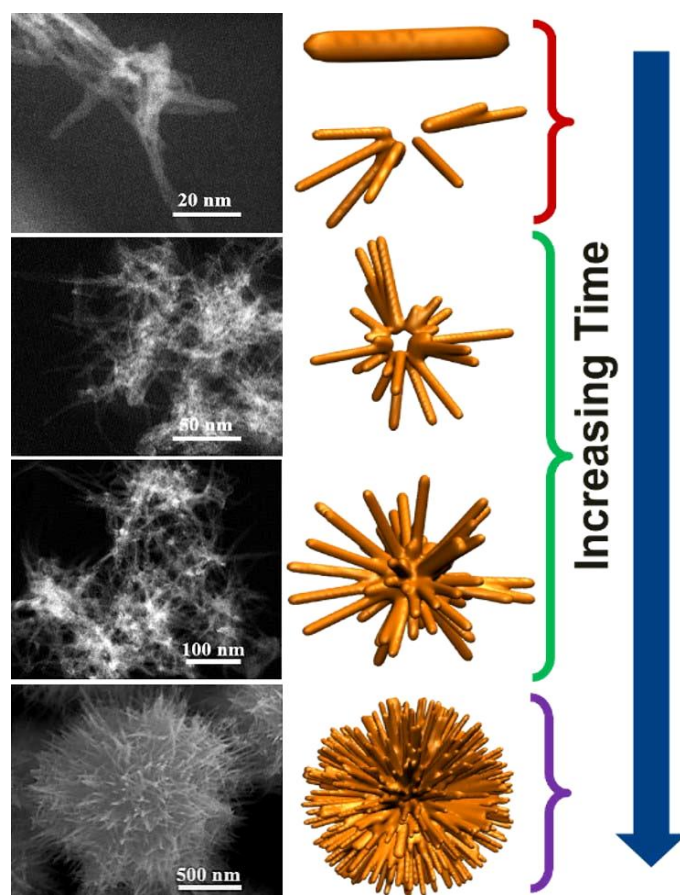
**Figure S7.** SEM and TEM images of CdS self-assembled nanostructures obtained after incubation at room temperature for one day initially, and then after incubation at 160 °C for different reaction times: (a, b) 20 min; (c, d) 40 min; (e, f) 60 min; (g, h) 80 min;  $V_R = 1.0$ .



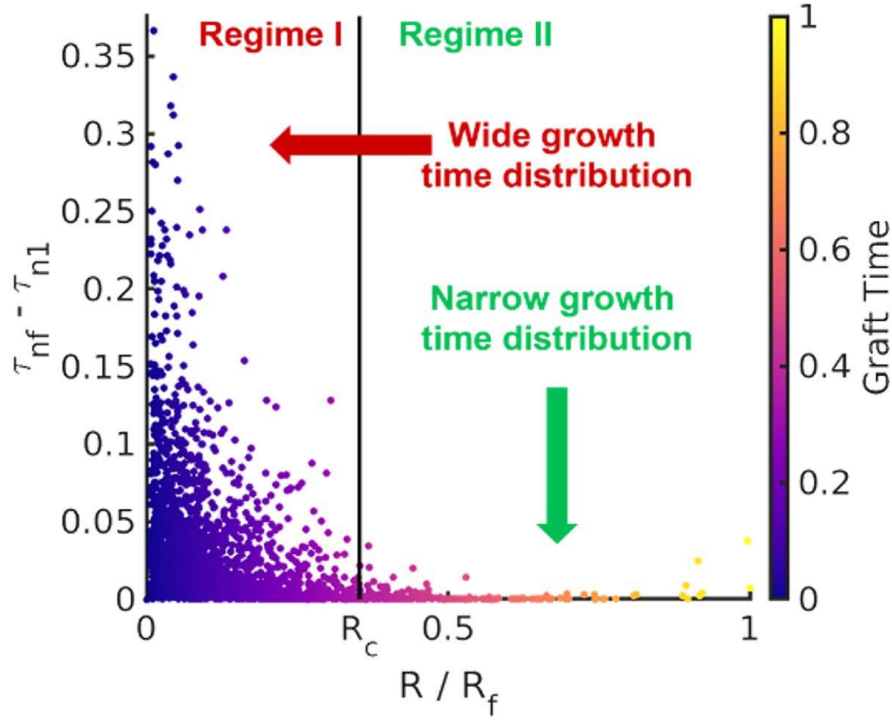
**Figure S8.** Time-dependent growth of CdS HPs obtained at 160 °C by naturally cooling down after (a) 25 min; (b) 2 h; (c) 4 h; (d) 5 h reaction times.



**Figure S9.** SEM images of CdS nanostructures obtained at 160 °C for 45 min with  $V_R = 1.0$ . Scale bars are all 50 nm.

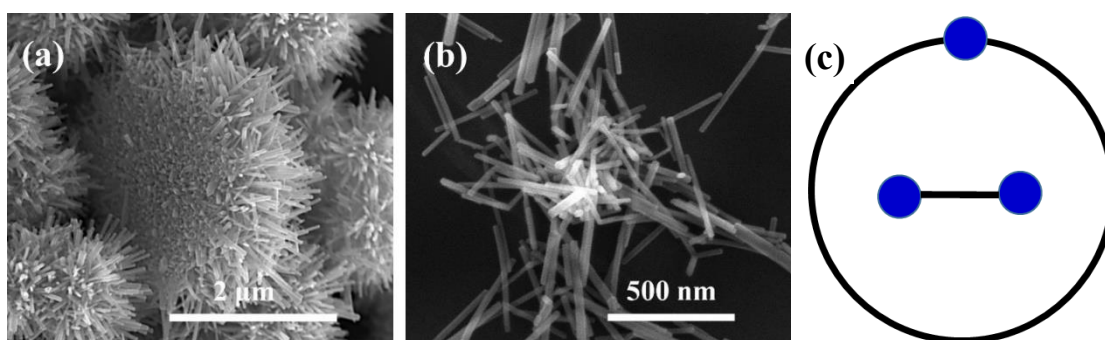


**Figure S10.** Comparison of experiments and simulation for temporal evolution of complex nanostructured microparticles.

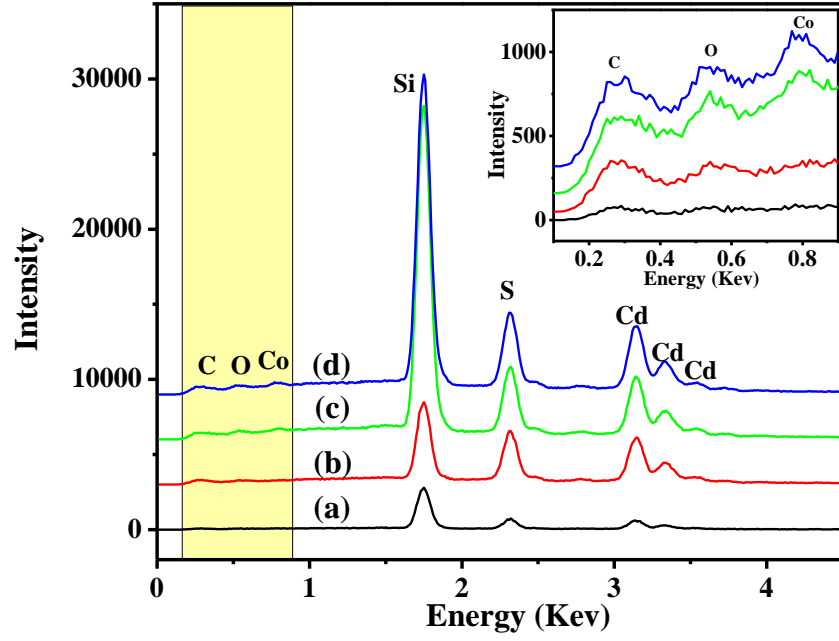


**Figure S11.** Growth time distribution of spikes on nanostructured microparticles. Figure S11 shows time difference between the first NP attachment time for a given spike and the last NP attachment time for the same spike as a function of growing SP. Each scatter point indicates a different spike on the SPCS. For clarity, we define  $\tau_{n1}$  as the time of 1<sup>st</sup> NP attachment for a given spike,  $\tau_{nf}$  as the time of last NP attachment for a given spike,  $R_c$  is the critical core size where electrostatics starts to compete with vdW,  $R$  is the size of the growing microparticle, and  $R_f$  is the final size of the nanostructured microparticle. Here, times are scaled such that 0 is at the beginning of the simulation and 1 is the end of the simulation, as indicated by the color bar.

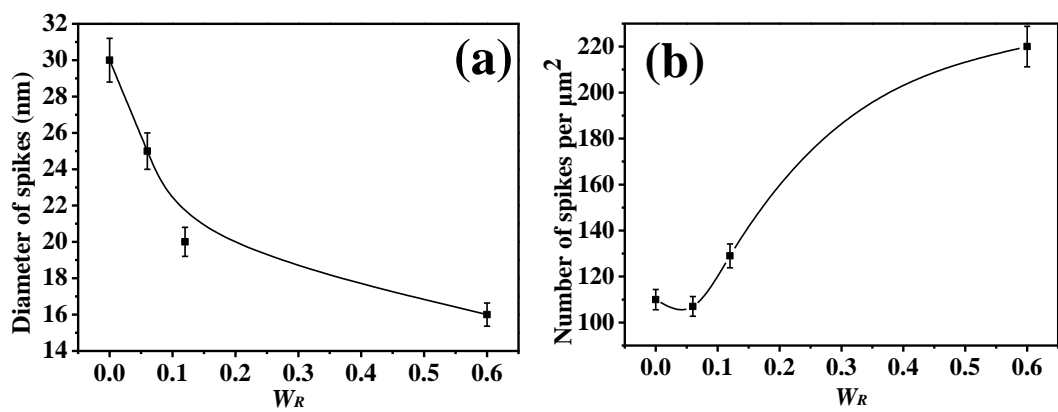
**Comment:**  $\tau_{nf} - \tau_{n1}$  exponentially decreases with increasing microparticle size  $R$ . With small  $R$ , the time spread is large, spanning anywhere from 10% – 35% of the total simulation time for each spike. This high distribution means that multiple spikes can concurrently grow in parallel or adjacent to each other. Doing so will result in higher chances for spikes to grow into each other's path, resulting in spike merging and amorphous aggregates as observed in experiments. This regime is expected when the effect of charge repulsion is low, allowing vdW to facilitate concurrent growths. Indeed, when the  $R$  becomes larger than the critical core size  $R_c$  ( $R > R_c$ ), we observe an immediate narrowing of the time difference. Here, electrostatics dominate. Each new spike rapidly grows to its final length as it is more energetically favorable to grow outward due to less charge repulsion as compared to concurrently growing multiple spikes (the reverse is true in the  $R < R_c$  regime). This shift is manifested in the well-formed, visually distinguishable spikes observed on the surface of fully formed HPs. The spike's final length is determined by the system lacking NPs of a sufficiently small enough size to continue growing.



**Figure S12.** Understanding the structure of the core in HPs. **(a)** SEM of the inner part of HPs visualized after cross-sectional ion beam milling of the particle. **(b)** CdS NRs separated from the core by sonication of the HPs. The length of the NRs is similar to the length of the spikes of HPs. **(c)** The GT representation only of the SP core of HPs (i.e. ignoring spikes). CdS NRs, represented by the  $K_2$  graph form size-limited self-assembled particle with a nearly random distribution of constituent monocrystalline NRs inside the particle. The SP graph also describes the structure of the SPCS in **Figure 8** where it is represented pictorially with the exception that all the NPs are assumed to form NRs represented by  $K_2$  in the center of the loop. If they would remain the single particle, they would be represented by  $K_1$ .



**Figure S13.** EDX of CdS-Co<sub>3</sub>O<sub>4</sub> HPs assembled at different  $W_R$  at 160 °C for 20 h: (a, black)  $W_R = 0.0$ ; (b, red)  $W_R = 0.06$ ; (c, green)  $W_R = 0.12$ ; (d, blue) 0.60.  $W_R$  is the weight ratio of Co<sub>3</sub>O<sub>4</sub> to CdS.



**Figure S14.** (a) Diameter and (b) areal density of  $\text{CdS-Co}_3\text{O}_4$  spikes.  $W_R$  is the weight ratio of  $\text{Co}_3\text{O}_4$  to  $\text{CdS}$ .